Directional, Horizontal Inhomogeneities of Cloud Optical Thickness Fields Retrieved from Ground-Based and Airborne Spectral Imaging

Michael Schäfer[1], Eike Bierwirth[1,2], André Ehrlich[1], Evelyn Jäkel[1], Frank Werner[3], and Manfred Wendisch[1]

[1]Leipzig Institute for Meteorology, University of Leipzig, Leipzig, Germany
[2]now at: PIER-ELECTRONIC GmbH, Nassaustr. 33–35, 65719 Hofheim-Wallau, Germany
[3]Joint Center for Earth Systems Technology, University of Maryland, 5523 Research Park Drive 320, Baltimore, MD 21228

Correspondence to: Michael Schäfer (michael.schaefer@uni-leipzig.de)

Abstract. Clouds exhibit significant horizontal inhomogeneities of their optical and microphysical properties, which complicate their realistic representation in weather and climate models. In order to investigate the directional, horizontal structure of cloud inhomogeneities, two-dimensional (2D) horizontal fields of optical thickness of subtropical cirrus and Arctic stratus with a spatial resolution of

5   < 10 m are investigated. The cloud optical thickness fields were derived from downward (transmitted) solar spectral radiance measurements from the ground beneath four cirrus clouds, and upward (reflected) radiances measured from aircraft above ten Arctic stratus clouds. The data were collected during the two major field campaigns Clouds, Aerosol, Radiation, and tuRbulence in the trade wInd regime over BArbados (CARRIBA) and VERical Distribution of Ice in Arctic clouds (VERDI).

10   Scalar one-dimensional (1D) and 2D autocorrelation functions, as well as power spectral densities are derived from the retrieved τ fields. Decorrelation lengths and scale breaks are identified and used to characterize the size range of the inhomogeneities and their influence on three-dimensional (3D) radiative effects. These studies reveal that there are considerable directional cloud inhomogeneities along and across the prevailing cloud structures. Therefore it is not sufficient to quantify horizon-

15   tal cloud inhomogeneities by scalar 1D inhomogeneity parameters; 2D parameters are necessarily required.

1   Introduction

The globally and annually averaged cloud cover is about 70 % (Rossow and Schiffer, 1999). Therefore, clouds need to be considered as an important regulator of the Earth's radiation budget (Albrecht,

20   1989; Loeb et al., 2009). Clouds scatter and absorb solar radiation in the wavelength range from 0.2 to 5 µm; they emit and absorb terrestrial radiation in the wavelength range from 5 to 50 µm. Although clouds have been studied for several decades, they are still poorly represented in weather and climate models (Shonk et al., 2011). The latest report of the Intergovernmental Panel on Climate Change (IPCC, 2013) classifies cloud effects as one of the largest uncertainties in climate

25   simulations, significantly contributing to problems in the determination of the Earth's energy budget (Stocker et al., 2013). These issues partly arise from an unrealistic representation of complex horizontal cloud structures and from cloud-radiation feedback processes that control the cloud evolution (Stephens, 2005; Shonk et al., 2011). Therefore, the representation of cloud inhomogeneities needs to be made more realistic (Shonk et al., 2011). This is particularly important, because changes of

30   cloud properties have important consequences on the interaction of clouds with radiation (Slingo, 1990).

High ice clouds (cirrus) and Arctic stratus exhibit significant horizontal inhomogeneities at different horizontal scales. Both cloud types can either warm or cool the climate system, depending on their optical and microphysical properties and the meteorological conditions. For example,

35   Choi and Ho (2006) reported for tropical regions a positive (warming) net radiative effect of cirrus with a cirrus optical thickness (τ_{ci}) of less than 10, but a cooling effect for $\tau_{ci} > 10$. For Arctic stratus, Wendisch et al. (2013) showed that for low surface albedo (α_s) and low solar zenith angle (θ_0), the cloud cools the sub-cloud layer. With increasing α_s and increasing θ_0, the cooling effect of the low–level cloud turns into a warming. Thus, the radiative forcing of cirrus and Arctic stratus is a function

40   of cloud optical thickness and the surface albedo. However, both, clouds and surface properties can vary significantly and in different horizontal scales. For example, in the cases of cirrus, Carlin et al. (2002) found a variability of cirrus albedo of up to 25 % due to spatial cirrus inhomogeneity. For Arctic stratus over variable sea-ice surfaces, Rozwadowska and Cahalan (2002) reported a plane-parallel albedo bias magnitude of less than 2 %, but an absolute value of the transmittance bias that

45   can exceed 10 %.

However, in most climate simulations and remote-sensing applications clouds are assumed as plane-parallel (Francis et al., 1998; Iwabuchi and Hayasaka, 2002; Garrett et al., 2003), which introduces biases into the modeled radiation budget (Shonk et al., 2011). Several studies investigated the influence of a plane-parallel assumption on cloud retrievals (e.g. Cahalan, 1994; Loeb and Davies,

50   1996; Marshak et al., 1998; Zinner et al., 2006; Varnai and Marshak, 2007). They found that the model biases are related to the degree of horizontal photon transport, which is ignored in radiative transfer schemes used in general circulation models (GCM). In 1D radiative transfer simulations clouds are divided into independent columns with horizontal homogeneous optical and microphysical properties (independent pixel approximation, IPA). However, horizontal photon transport can-

55   not be neglected in case of inhomogeneous clouds. The multiple scattering due to 3D microphysical cloud structures smooth the sampled radiation field. On small scales, this limits the accuracy

Atmospheric
Chemistry
and Physics
Discussions

of IPA. Cahalan (1994) and Marshak et al. (1995) revealed discrepancies for individual pixel radiances exceeding 50 %. For the top-of-atmosphere cloud radiative forcing (solar and terrestrial), Shonk and Hogan (2008) reported an overestimation of about 8 % caused by horizontal inhomogeneities of cloud microphysical parameters.

3D Monte Carlo radiative transfer simulations account for the horizontal photon transport (Barlakas et al., 2016). However, they are costly in terms of computation time and memory (Huang and Liu, 2014). This renders Monte Carlo radiative transfer simulations inappropriate for the application in operational or global models. Other approaches introduce cloud overlap schemes (COS), such as the maximum-random COS (Geleyn and Hollingsworth, 1979), the exponential-random COS (Hogan and Illingworth, 2000), or Triplecloud COS (Shonk and Hogan, 2008). Improvements compared to the plane-parallel assumption are achieved, but results are still not as accurate as achieved from 3D Monte Carlo methods or measurements. To reduce uncertainties associated with 1D plane-parallel assumptions, Huang and Liu (2014) apply spatial autocorrelation functions of cloud extinction coefficients to capture the net effects of subgrid cloud interactions with radiation. With several orders less computation time, this approach reproduces 3D Monte Carlo radiative transfer simulations with a sufficient accuracy within 1 %. However, the method requires spatial autocorrelation functions of cloud extinction coefficients with high spatial resolution, which underlines the need for measurements of comparable resolution.

GCM or numerical weather forecast models such as that from the European Centre for Medium-Range Weather Forecasts (ECMWF) require sub-grid scale parameterizations of, e.g., cloud structures, liquid water content (LWC), and/or ice water content (IWC) (Huang and Liu, 2014). Cloud structures including inhomogeneities show spatial features down to distances below the meter scale (Pinsky and Khain, 2003). Therefore, measurements with appropriate spatial and temporal resolution have to be conducted to obtain the parameterizations. The required measurements include cloud altitude (temperature), its geometry (vertical and horizontal extent), and cloud microphysical properties (e.g., LWC, IWC, droplet size, ice crystal size and shape distributions).

The structure of cloud inhomogeneities may exhibit a prevailing directional character (e.g., induced by the prevailing wind). 1D observations with LiDAR (light detecting and ranging) or point spectrometers can lead to unrealistic results of the degree of horizontal cloud inhomogeneity. For example, a cloud, which exhibits a rather inhomogeneous character may be classified as horizontally homogeneous, if the prevailing directional structure has the same orientation as the path of measurements alongside the cloud. In this regard, 2D observations are a useful tool to avoid such misinterpretations of cloud inhomogeneity.

Horizontal τ fields retrieved from spectral solar radiance measurements are analyzed to quantify horizontal inhomogeneities of two cloud types; cirrus and Arctic stratus. The statistical evaluation of the horizontal inhomogeneity of the fields of τ applies scalar 1D inhomogeneity parameters from the literature (Sect. 3), 2D autocorrelation functions (Sect. 4), and 2D Fourier analysis (Sect. 5).

2 Data Set: 2D-Fields of Cloud Optical Thickness

95   Data from two international field campaigns have been analyzed: the Clouds, Aerosol, Radiation, and tuRbulence in the trade wInd regime over BArbados (CARRIBA, Siebert et al., 2013; Schäfer et al., 2013) campaign performed on Barbados in April 2011, and the VERical Distribution of Ice in Arctic clouds (VERDI, Schäfer et al., 2015) observations carried out in Inuvik, Canada in May 2012. Downward and upward solar spectral radiances ($I_\lambda^\downarrow$, $I_\lambda^\uparrow$) were measured from the ground

100   (CARRIBA) and from an aircraft (VERDI). The instrument applied during the measurements was the imaging spectrometer AisaEAGLE (manufactured by Specim Ltd., Finland, Hanus et al., 2008; Schäfer et al., 2013, 2015), which is a single–line sensor with 1024 spatial pixels detecting radiation in the wavelength range from 400 nm to 970 nm with a spectral resolution of 1.25 nm full with at half maximum (FWHM). The instrument was carefully characterized and calibrated in the laboratory to

105   transform the AisaEAGLE's raw data (12-bit digital numbers) into radiance. The procedure of data evaluation (calibrations, corrections) follows the methods described by Bierwirth et al. (2013) and Schäfer et al. (2013, 2015).

The ground-based and airborne measured fields of $I_\lambda^\downarrow$ (CARRIBA) and $I_\lambda^\uparrow$ (VERDI) were used to retrieve horizontal fields of τ with a spatial resolution of < 10 m. Detailed descriptions and sen-

110   sitivity tests of the applied retrieval procedures are reported by Schäfer et al. (2013) for cirrus and by Bierwirth et al. (2013) as well as Schäfer et al. (2015) for Arctic stratus. Fields of cloud optical thickness are derived for four cirrus cases (τ_{ci}) and ten Arctic stratus cases (τ_{st}). Subsequently, those fields of τ_{ci} and τ_{st} are used to investigate and quantify horizontal cloud inhomogeneities.

As proposed by Marshak et al. (1995), Oreopoulos et al. (2000), or Schroeder (2004), horizontal

115   cloud inhomogeneities are usually studied by scale analysis of cloud-top reflectances. However, radiance measurements include the information of the scattering phase function, imprinted in the measured fields of radiance (Schäfer et al., 2013). To avoid artifacts in the scale analysis resulting from such features, parameters that account for the directional scattering of the cloud particles in the retrieval algorithm have to be analyzed. Accounting for the directional scattering of the cloud

120   particles in the retrieval algorithm, τ does theoretically not include the footprint of the scattering phase function. Therefore, in the following, the retrieved fields of τ_{ci} and τ_{st} are used to investigate and quantify horizontal cloud inhomogeneities of cirrus and Arctic stratus.

Table 1 summarizes the statistical parameters of the four retrieved fields of τ_{ci} (C-01 to C-04) and the ten retrieved fields of τ_{st} (V-01 to V-10). Figure 1 illustrates example cutouts for cases V-04 and

125   V-07, both characterized by a measurement duration of 60 s. Table 1 further provides information on the measurement time, cloud altitude (h_{cld}), field size (swath, length), and average as well as standard deviation of τ_{ci} ($\bar{\tau}_{ci} \pm \sigma_{\tau,ci}$) and τ_{st} ($\bar{\tau}_{st} \pm \sigma_{\tau,st}$). The sampled cirrus fields of about 13-44 km length and 7-8 km width are determined by the observation time and the swath covered by AisaEAGLE. For the Arctic stratus cases the average swath of the covered cloud fields has a size close to 1.3 km.

130   The length varies from 4 km to up to 26 km. Thus, for CARRIBA and VERDI sufficiently large

Atmospheric
Chemistry
and Physics

Open Access

EGU

Discussions

areas of the clouds are covered to provide a statistically firm analysis of τ_{ci} and τ_{st} and to investigate horizontal inhomogeneities in the fields of τ_{ci} and τ_{st}.

Table 1. Label, measurement period (day and time of day in UTC), cloud top altitude, swath, length, and average and standard deviation ($\bar{\tau} \pm \sigma_\tau$) of the retrieved fields of τ_{ci} and τ_{st} from ground-based measured CARRIBA (C-01 to C-04) and airborne measured VERDI (V-01 to V-10) cases. The flight altitude for each VERDI case is at 2920 m. The last three columns include calculated scalar 1D inhomogeneity parameters (ρ_τ, S_τ, χ_τ) of the retrieved fields of τ. They are discussed in Sect. 3.

Case	Day	Time (UTC)	h_{cld} (km)	Swath (km)	Length (km)	$\bar{\tau} \pm \sigma_\tau$	ρ_τ	S_τ	χ_τ
C-01	9 April 2011	13:26:26 – 13:37:13	11-15	7.3	15.6	0.41 ± 0.17	0.40	0.19	0.92
C-01	16 April 2011	13:44:29 – 14:17:42	12-15	8.0	40.5	0.28 ± 0.09	0.35	0.15	0.94
C-01	18 April 2011	13:43:56 – 14:17:13	13-15	8.6	44.1	0.20 ± 0.03	0.17	0.08	0.99
C-01	23 April 2011	16:45:10 – 17:03:12	11-14	7.3	13.3	0.05 ± 0.04	0.91	0.48	0.63
V-01	14 May 2012	20:31:47 – 20:36:31	≤ 0.90	1.34	21.28	9.93 ± 1.89	0.19	0.08	0.98
V-02	14 May 2012	20:38:04 – 20:42:09	≤ 0.85	1.37	20.83	7.82 ± 2.01	0.26	0.11	0.97
V-03	14 May 2012	20:53:26 – 20:58:30	≤ 0.85	1.37	26.85	3.82 ± 1.33	0.34	0.20	0.92
V-04	15 May 2012	18:41:53 – 18:43:58	≤ 1.00	1.27	10.50	14.34 ± 2.54	0.18	0.08	0.98
V-05	15 May 2012	21:05:10 – 21:09:24	≤ 0.93	1.32	20.22	6.35 ± 0.97	0.15	0.07	0.99
V-06	16 May 2012	19:10:56 – 19:15:56	≤ 1.00	1.27	23.10	6.52 ± 1.48	0.23	0.11	0.97
V-07	17 May 2012	16:53:23 – 16:56:06	≤ 0.25	1.75	12.74	3.04 ± 0.66	0.22	0.11	0.97
V-08	17 May 2012	17:00:59 – 17:06:15	≤ 1.00	1.27	25.65	5.48 ± 1.84	0.34	0.15	0.95
V-09	17 May 2012	17:09:28 – 17:10:38	≤ 2.25	0.48	5.46	7.07 ± 1.41	0.20	0.09	0.98
V-10	17 May 2012	18:49:26 – 18:50:16	≤ 0.23	1.76	4.10	4.15 ± 0.67	0.16	0.08	0.99

3 Scalar 1D Inhomogeneity Parameters

The standard deviation σ_τ of the cloud optical thickness does not allow a comparison between different cases with different average cloud optical thickness $\bar{\tau}$. A cloud with higher $\bar{\tau}$ can naturally exhibit a higher standard deviation. Therefore, Davis et al. (1999) and Szczap et al. (2000) used the normalized inhomogeneity measure ρ_τ to quantify the horizontal inhomogeneity of τ. It is defined by the ratio of σ_τ and the average value $\bar{\tau}$ of the corresponding sample:

$$\rho_\tau = \frac{\sigma_\tau}{\bar{\tau}}. \tag{1}$$

An absolutely homogeneous cloud is characterized by $\rho_\tau = 0$. Increasing values of ρ_τ indicate increasing cloud inhomogeneity. However, the fact that ρ_τ can exceed values of unity and depends on the average value might lead to misinterpretations. Therefore, Davis et al. (1999) and Szczap et al.
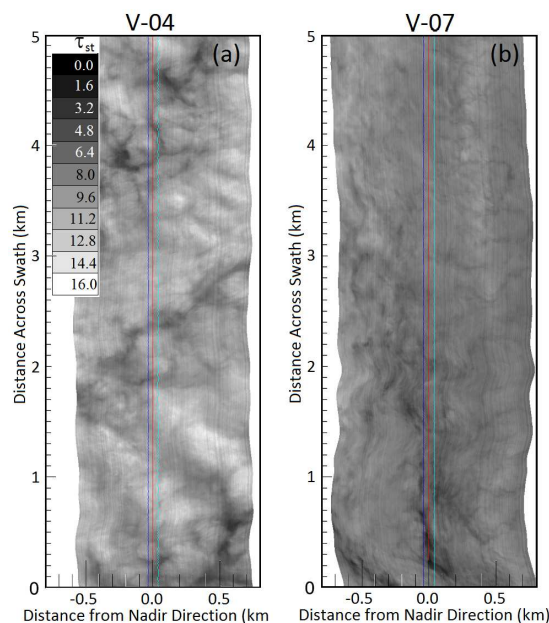
Figure 1. (a) Georeferenced field of τ_{st}. Cutout from measurement case V-04 with 60 s measurement duration. The dark–blue, red, and light–blue lines illustrate the nadir viewing direction in a range of $\pm 1°$. **(b)** Same as (a) for case V-07.

(2000) convert the relative variability ρ_τ into the inhomogeneity parameter S_τ as follows:

$$S_\tau = \frac{\sqrt{\ln(\rho_\tau^2 + 1)}}{\ln 10}.$$ (2)

145   In case of a log-normal frequency distribution of τ, S_τ is linearly proportional to to ρ_τ. This is because the reflected/transmitted radiance is approximately linear to $\log \tau$ for moderate τ (for $\log \tau = 0.5\text{-}1.5$ with $\tau \approx 3\text{-}30$). Without net horizontal photon transport, moments of reflected/transmitted radiance are closely associated with moments of $\log \tau$ rather than moments of τ (Iwabuchi and Hayasaka, 2002). Therefore, S_τ quantifies the degree of cloud inhomogeneity.

150   Oreopoulos and Cahalan (2005) investigated the inhomogeneity parameter χ_τ, first introduced by Cahalan (1994). χ_τ is defined as the ratio of the logarithmic and linear average of a distribution of $\bar{\tau}$:

$$\chi_\tau = \frac{\exp(\overline{\ln \tau})}{\bar{\tau}},$$ (3)

χ_τ ranges between 0 and 1, with values close to unity indicating horizontal homogeneity, and val-
155   ues approaching zero characterizing high horizontal inhomogeneity. Oreopoulos and Cahalan (2005) state that the reflected solar flux is approximately a linear function of the logarithm of τ for a wide

Atmospheric
Chemistry
and Physics
Discussions

range of τ (≈ 3 to ≈ 30, depending on θ_0). Thus, the logarithmically averaged τ provides a way to account for cloud inhomogeneity effects in plane-parallel radiative transfer calculations by including the nonlinear nature of the relation between τ and cloud albedo.

160   The three scalar 1D inhomogeneity parameters ρ_τ, S_τ, and χ_τ are calculated for each retrieved field of τ_{ci} and τ_{st} from the CARRIBA and VERDI campaigns. The results are listed in the last three columns of Tab. 1.

    The cirrus cases observed during CARRIBA show ρ_τ in the range of 0.17–0.91, while S_τ is in the range of 0.08–0.48. The largest values of ρ_τ and S_τ are found for C-04, the lowest for C-03. The val-
165 ues for ρ_τ and S_τ show that the cirrus of C-02 and C-03 was quite homogeneous and that of C-01 and C-04 was rather inhomogeneous. For the ten Arctic stratus cases, ρ_τ and S_τ are in the range of 0.15–0.34 and 0.07–0.20, respectively. For stratocumulus Zuidema and Evans (1998) quantified the inhomogeneity of τ with $S_\tau = 0.1$–0.3. Iwabuchi (2000) and Iwabuchi and Hayasaka (2002) investigated the inhomogeneity of τ for overcast boundary layer clouds and found values of $S_\tau = 0.03$–0.3, which
170 leads to $\rho_\tau = 0.07$–0.78. Thus, the derived values from CARRIBA and VERDI compare well with the values reported by Zuidema and Evans (1998), Iwabuchi (2000), and Iwabuchi and Hayasaka (2002). Among all ten cases, ρ_τ and S_τ indicate case V–03 and V–08 to be more inhomogeneous.

    For CARRIBA, the values of χ_τ range from 0.63 to 0.99, indicating a rather inhomogeneous cirrus for C-04 and quite homogeneous cirrus during the other days. In contrast to the results for
175 ρ_τ and S_τ, χ_τ indicates that the cirrus of C-01 is less inhomogeneous. The calculated values of χ_τ for the retrieved fields of τ_{st} from the VERDI campaign yield values larger than 0.9 in each case, with lowest values for case V-03 and V-08, which were already indicated by ρ_τ and S_τ to be more inhomogeneous. Depending on cloud type, cloud phase, surface type, season, and time of day, Oreopoulos and Cahalan (2005) estimate the range of χ_τ from ≈ 0.65 to 0.8.

180   The comparison to literature values shows that the derived scalar 1D inhomogeneity parameters ρ_τ, S_τ, and χ_τ are suitable to characterize the general character of clouds with regard to their inhomogeneities. They are easy to calculate and suitable for being implemented in simulations that assume horizontally homogeneous clouds to achieve more realistic results. ρ_τ, S_τ, and χ_τ do not provide a measure of the directional variability of the inhomogeneities. However, different cloud
185 types exhibit horizontal inhomogeneities of different size and orientation. For example, the observed clouds from the CARRIBA and VERDI campaigns are different in most aspects (e.g. cloud altitude, cloud structure, cloud phase, particle size and shape), but ρ_τ, S_τ, and χ_τ yield comparable values (compare Fig. 1 with scalar 1D inhomogeneity parameters listed in Tab. 1). Therefore, in order to characterize cloud inhomogeneities of different cloud types not only the scalar horizontal inhomo-
190 geneity but also its directional dependence needs to be investigated (Hill et al., 2012).

4 Spatial 1D and 2D Autocorrelation Functions and Decorrelation Length

The 2D autocorrelation function $P_\tau(L_x, L_y)$ is calculated in both dimension at fixed distances (pixel-lags) L_x and L_y, which are derived as integer multiples of the equidistant sample intervals x_j and y_k of the 2D fields of τ (Marshak et al., 1998). The maximum pixel-lags L_x and L_y are given by the number of pixels n and m of the 2D fields. Here, with n and m equidistant measurement intervals x_j and y_k, $P_\tau(L_x, L_y)$ for 2D fields of τ is calculated by:

$$P_\tau(L_x, L_y) = \frac{\sum\limits_{j,k+1}^{n,m} [\tau(x_j + L_x, y_k + L_y) - \bar{\tau}] \cdot [\tau(x_j, y_k) - \bar{\tau}]}{\sum\limits_{j,k+1}^{n,m} [\tau(x_j, y_k) - \bar{\tau}]^2}. \tag{4}$$

$\tau(x_j, y_k)$ is the cloud optical thickness observed at the reference position, and $\tau(x_j + L_x, y_k + L_y)$ is the cloud optical thickness at pixel-lag L_x and L_y. $P_\tau(L_x, L_y)$ yields values between -1 and 1, 1 representing a perfect positive correlation (e.g., for a spatial shift equal to zero); a value of -1 is a perfect negative correlation and 0 indicates no correlation. Thus, spatial autocorrelation functions measure the degree of similarity between spatially distributed neighbouring samples. By nature, τ values in close horizontal distance show similar values, while cloud pixels at larger distances can show significantly different τ, depending on the cloud heterogeneity. To avoid ambiguous results with respect to positive and negative correlations, the squared autocorrelation function $P_\tau^2(L_x, L_y)$ is used, because it yields values between 0 (no correlation) and 1 (perfect correlation) only.

Figures 2b and 2d show examples of $P_\tau^2(L_x, L_y)$ color-coded in a 2D plot for $L_x = -250$ to $L_x = 250$ and $L_y = -250$ to $L_y = 250$, calculated for a selected area (500 by 500 Pixels, Figs.2a and 2b) of the entire fields from case C-01 and C-03 with $L_x = 250$ and $L_y = 250$. The positive and negative signs have no physical meaning, they illustrate the shifting direction only. Both cases show a different pattern of $P_\tau^2(L_x, L_y)$ with increasing absolute value of L_x and L_y. While C-01 shows a circular spot indicating a symmetry independent on direction, C-03 displays high correlation factors for all considered L_y within a range of $L_x=-50$ to $L_x=50$. This pattern indicates a homogeneous cloud structure along the y axis while the τ field along the x-axis is heterogeneous. The magnitude of decrease of $P_\tau^2(L_x, L_y)$ with increasing L_x and L_y depends on the horizontal structure of the cloud inhomogeneities. The $P_\tau^2(L_x, L_y)$ calculated from C-01 (Fig. 2b) show a decrease, independent of the direction. In contrast, the $P_\tau^2(L_x, L_y)$ calculated from C-03 (Fig. 2d) show a directional dependence.

The squared spatial autocorrelation functions $P_\tau^2(L_x, L_y)$ are used to calculate the decorrelation length $\xi_\tau = \sqrt{L_x^2 + L_y^2}$ with:

$$P_\tau^2(\xi_\tau) = 1/e. \tag{5}$$

ξ_τ quantifies a length scale (in units of meter) where individual cloud parcels are decorrelated and provides a measure of the horizontal extent of cloud inhomogeneities. Strong inhomogeneities correspond to small ξ_τ. In Figs. 2b and 2d, ξ_τ is indicated by a white line. For C-01 ξ_τ forms
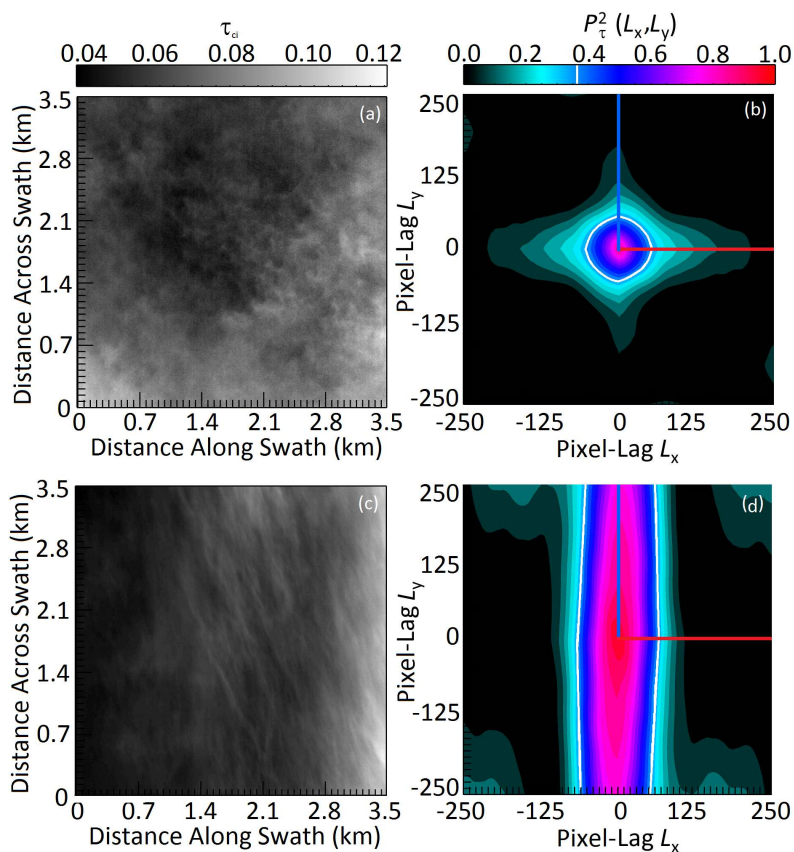
Figure 2. (a) Selected cloud scene (3.5 km by 3.5 km) of field of τ_{ci} from case C-01. **(b)** Color-coded 2D field of $P_\tau^2(L_x, L_y)$, calculated for field of τ_{ci} from (a). The blue and red line illustrate the pixel-lags selected for the illustration in Fig. 3a. The white line illustrates ξ_τ at $P_\tau^2(L_x, L_y) = 1/e$. **(c)** Same as (a) for case C-03. **(d)** Same as (b) for selected τ_{ci} field shown in (c).

a circular shape indicating a similar magnitude of cloud inhomogeneities in all directions of the

225   cloud field. Conversely, for C-03 ξ_τ along pixel-lag L_x is significantly smaller than ξ_τ along pixel-lag L_y. This directional dependence is related to the structure of the cloud with regular filaments in the swath direction of the image in Fig. 2c. For case C-01 the symmetry in $P_\tau^2(L_x, L_y)$ means that the cloud inhomogeneity can be characterized by a single ξ_τ, independent of direction. For regularly structured clouds such as C-03, however, the 2D decorrelation can be split into a component of the

230   largest variability and a component along the smallest variability of τ. In the cloud fields presented here, both major axes align with the x and y direction. 1D autocorrelation functions along the axis of strongest ($\leftrightarrow$, red line in Figs. 2b and 2d) and weakest ($\updownarrow$, blue line in Figs. 2b and 2d) variability
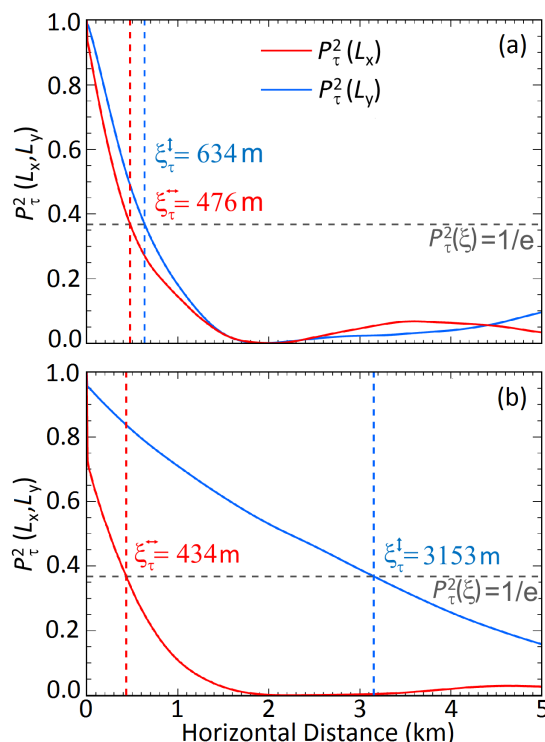
Figure 3. (a) Average $P_\tau^2(L_x, L_y)$ (solid lines) and derived ξ_τ (dotted lines) along L_x (blue) and L_y (red) from Fig. 2b. (b) Same as (a) for $P_\tau^2(L_x, L_y)$ shown in Fig. 2d.

are provided in Figs. 3a and 3b. To derive quantitative values for $\xi_\tau^{\leftrightarrow}$ and $\xi_\tau^{\updownarrow}$ in SI-units of meter, the pixel-lag is transformed into horizontal distances by multiplying the number of pixels by their pixel

235   size.

For case C-01 (Figs. 2a, 2b, and 3a), the derived $P_\tau^2(L_x, L_y)$ along and across the prevailing directional structure are similar and $\bar{\xi}_\tau^{\updownarrow} = 634\,\text{m}$ compares well with $\bar{\xi}_\tau^{\leftrightarrow} = 477\,\text{m}$ within the range of standard deviation given in Tab. 2. For case C-03 (Figs. 2c, 2d, and 3b), the $P_\tau^2(L_x, L_y)$ along and across the prevailing directional structure differ significantly from each other and $\bar{\xi}_\tau^{\updownarrow} = 3154\,\text{m}$

240   is about seven times larger than $\bar{\xi}_\tau^{\leftrightarrow} = 434\,\text{m}$. Thus, for clouds with a prevailing directional structure it is advisable to give variable ξ_τ as a function of observation direction, e.g., by two parameters, $\xi_\tau^{\updownarrow}$ along and $\xi_\tau^{\leftrightarrow}$ across the prevailing cloud structure.

Table 2 summarizes and Fig. 4 illustrates the resulting $\bar{\xi}_\tau^{\leftrightarrow}$ and $\bar{\xi}_\tau^{\updownarrow}$ of all measurement cases from CARRIBA and VERDI. Additionally, $\bar{\xi}_\tau \pm \sigma_\xi$ are included ($\bar{\xi}_\tau^{\updownarrow} \pm \sigma_\xi, \bar{\xi}_\tau^{\leftrightarrow} \pm \sigma_\xi$) in Tab. 2. Those values

Atmospheric
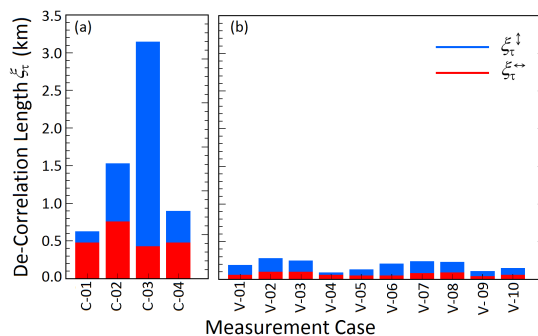Chemistry
and Physics

Discussions

Open Access

Figure 4. Decorrelation length calculated for the retrieved fields of τ from the **(a)** CARRIBA (C-01–C-04) and **(b)** VERDI (V-01–V-10) campaigns. Vertical arrows ($\updownarrow$) indicate the calculation of $P_\tau^2(L_x, L_y)$ and subsequent derivation of ξ_τ along L_y, horizontal arrows ($\leftrightarrow$) along L_x.

245 illustrate the pixel by pixel variability for all calculated $P_\tau^2(L_x, L_y)$ along one direction. Due to the exponential behavior of $P_\tau^2(L_x, L_y)$ they are asymmetric with respect to $\bar{\xi}_\tau^{\updownarrow}$ and $\bar{\xi}_\tau^{\leftrightarrow}$.

Table 2. Decorrelation length calculated for the retrieved fields of τ from the CARRIBA (C-01–C-04) and VERDI (V-01–V-10) campaigns. Vertical arrows ($\updownarrow$) indicate the calculation of $P_\tau^2(L_x, L_y)$ and subsequent derivation of ξ_τ along L_y, horizontal arrows ($\leftrightarrow$) along L_x. $\bar{\xi}_\tau$ is the average of all pixels, $\bar{\xi}_\tau - \sigma_\xi$ is the average minus standard deviation, and $\bar{\xi}_\tau + \sigma_\xi$ is the average plus standard deviation.

Case	$\bar{\xi}_\tau^{\updownarrow} - \sigma_\xi$ (km)	$\bar{\xi}_\tau^{\updownarrow}$ (km)	$\bar{\xi}_\tau^{\updownarrow} + \sigma_\xi$ (km)	$\bar{\xi}_\tau^{\leftrightarrow} - \sigma_\xi$ (km)	$\bar{\xi}_\tau^{\leftrightarrow}$ (km)	$\bar{\xi}_\tau^{\leftrightarrow} + \sigma_\xi$ (km)
C-01	0.56	0.63	0.75	0.31	0.48	0.88
C-02	1.41	1.53	1.67	0.66	0.76	0.86
C-03	2.62	3.15	3.83	0.26	0.43	0.80
C-04	0.69	0.90	1.24	0.35	0.48	0.76
V-01	0.16	0.19	0.26	0.04	0.06	0.10
V-02	0.19	0.28	0.52	0.07	0.10	0.16
V-03	0.24	0.25	0.27	0.06	0.10	0.17
V-04	0.08	0.09	0.11	0.04	0.06	0.10
V-05	0.11	0.13	0.15	0.03	0.05	0.07
V-06	0.13	0.21	0.37	0.03	0.05	0.08
V-07	0.16	0.24	0.48	0.05	0.08	0.15
V-08	0.12	0.23	0.65	0.06	0.09	0.15
V-09	0.08	0.11	0.15	0.02	0.04	0.06
V-10	0.09	0.15	0.27	0.04	0.06	0.09

Atmospheric
Chemistry
and Physics
Discussions

For the cirrus clouds observed during CARRIBA, ξ_τ varies from $434\,\mathrm{m}$ to $3\,154\,\mathrm{m}$, depending on the cloud structure and inhomogeneity. The rather inhomogeneous cases C-01 and C-04 with highly variable τ_{ci} on small scales yield rapidly decreasing $P_\tau^2(L_{\mathrm{x}}, L_{\mathrm{y}})$ with low $\bar{\xi}_\tau$. In contrast, the quite homogeneous cases C-02 and C-03 yield slowly decreasing $P_\tau^2(L_{\mathrm{x}}, L_{\mathrm{y}})$ and larger $\bar{\xi}_\tau$. The differences between $\bar{\xi}_\tau^{\updownarrow}$ and $\bar{\xi}_\tau^{\leftrightarrow}$ reach up to $85\,\%$.

For the Arctic stratus fields observed during VERDI, $\bar{\xi}_\tau^{\updownarrow}$ and $\bar{\xi}_\tau^{\leftrightarrow}$ range between $35\,\mathrm{m}$ and $278\,\mathrm{m}$ and are significantly smaller (more inhomogeneous) than those for the cirrus clouds probed during CARRIBA, although the scalar 1D inhomogeneity parameters from Tab. 1 yield similar values. This illustrates that the scalar 1D inhomogeneity parameters ρ_τ, S_τ, and χ_τ are not well suited to compare different types of clouds. A comparison can only indicate differences with regard to the evaluation of the horizontal dependence of cloud inhomogeneities. Similar to the CARRIBA cirrus cases, the differences between $\bar{\xi}_\tau^{\updownarrow}$ and $\bar{\xi}_\tau^{\leftrightarrow}$ are significant reaching values of up to $77\,\%$.

5 Power Spectral Density Analysis

Multiple scattering in inhomogeneous 3D cloud structures causes a smoothing of the reflected I_λ above clouds (Cahalan and Snider, 1989; Marshak et al., 1995). This effect (especially multiple scattering in horizontal direction) generates uncertainties in the retrieved fields of τ if homogeneous plane-parallel clouds are assumed in the retrieval. The smoothing effect is analyzed using the Fourier transform of the retrieved fields of τ. The application of Fourier transforms for the investigation of cloud inhomogeneities is widely used in the existing literature (e.g., Cahalan, 1994; Davis et al., 1999; Schroeder, 2004). However, in most of these studies, the 1D Fourier transformation is adopted to narrow pixel-lines of radiative quantities such as I_λ or the reflectivity γ_λ. Here, a 2D Fourier transformation is applied to spatial 2D cloud scenes. Schäfer et al. (2013) showed that angular features of the scattering phase functions are imprinted in the I_λ measurements of AisaEAGLE. To avoid artifacts in the Fourier transform arising from those features, fields of τ are used for the analysis. Accounting for the directional scattering of the cloud particles in the retrieval algorithm, τ does theoretically not include the footprint of the scattering phase function if the correct particle size and shape are assumed.

The Fourier transformation decomposes a periodic function into a sum of sinusoidal base functions. For a given measurement, here $\tau(x, y)$, the 2D Fourier transform $\mathcal{F}_\tau(k_{\mathrm{x}}, k_{\mathrm{y}})$ is defined by:

$$\mathcal{F}_\tau(k_{\mathrm{x}}, k_{\mathrm{y}}) = \int\limits_{-\infty}^{\infty} \int\limits_{-\infty}^{\infty} \tau(x, y) e^{-2\pi i(k_{\mathrm{x}}x + k_{\mathrm{y}}y)} \, \mathrm{d}x \, \mathrm{d}y, \tag{6}$$

The base functions are described by a complex exponential of different frequency. The fields of τ are given as a function of horizontal distances x and y. Therefore, wave numbers $k_{\mathrm{x}} = 1/x$ and $k_{\mathrm{y}} = 1/y$ are used in the base functions.

The Fourier coefficients $\mathcal{F}_\tau(k_x, k_y)$ are calculated using a Discrete Fourier Transform (DFT). With n and m discrete elements in the x_j and y_k dimension of the τ field, the 2D DFT is derived by:

$$\mathrm{DFT}(k_x, k_y) = \frac{1}{n \cdot m} \sum_{x_j=0}^{n-1} \sum_{y_k=0}^{m-1} \tau(x_j, y_k) \cdot e^{-2\pi i \cdot \left(\frac{k_x x_j}{n} + \frac{k_y y_k}{m} \right)}. \tag{7}$$

Figures 5 and 6 present the Fourier transform in the form of power spectral densities $E(k_x)$ and $E(k_y)$, in the following called $E(k_x, k_y)$, calculated from the complex Fourier coefficients by:

$$E(k_x, k_y) = \mathrm{DFT}^2(k_x, k_y). \tag{8}$$

Figures 5a to 5c show τ_{ci} fields of three selected cloud areas of 3.5 km by 3.5 km size extracted from the cases C-01, C-02, and C-03. C-01 represents an inhomogeneous cirrus without a preferred direction in the cloud structure (Fig. 5a). In C-02 a homogeneous cirrus with a moderate directional structure (Fig. 5b) is selected, while in C-03 an inhomogeneous cirrus with a distinct directional structure (Fig. 5c) is presented. Figures 5d to 5f show the corresponding logarithm of the 2D power spectral densities $E(k_x, k_y)$. Largest values of $E(k_x, k_y)$ are found at smallest wave numbers k_x and k_y, which are located in the center of the image. In general the values of $E(k_x, k_y)$ decrease with increasing k_x and k_y. Inhomogeneous clouds (Figs. 5d and 5f) show higher values of $E(k_x, k_y)$ over a wide range of wave numbers k_x and k_y, whereas the dominating $E(k_x, k_y)$ for homogeneous clouds (Fig. 5e) are only located close to the smallest wave numbers k_x and k_y. Similar to the autocorrelation functions the decrease of $E(k_x, k_y)$ is rotationally symmetric for clouds with no preferred directional structure (Fig. 5d), but asymmetrical for clouds with a prevailing directional structure (Figs. 5e, 5f).

To quantify the two-dimensional nature of the symmetry, Figs. 5g to 5f show the $E(k_x, k_y)$ along (black, E_b) and across (red, E_a) the direction of the strongest symmetry axis. For the inhomogeneous case without a prevailing directional structure (C-01), both components E_a and E_b are almost identical. For the homogeneous case with a moderate directional structure (C-02), both E_a and E_b are similar over most of the covered range of k_x and k_y, except for the smallest wave number $k_x < 3\,\mathrm{km}^{-1}$ and $k_y < 3\,\mathrm{km}^{-1}$. For the inhomogeneous case with a distinct directional structure (C-03), both E_a and E_a are of similar magnitude only at $k_x > 7\,\mathrm{km}^{-1}$ and $k_y > 7\,\mathrm{km}^{-1}$. The differences in E_a and E_b of clouds with a prevailing directional structure result from the different k_x and k_y, at which the signal turns into white noise (constant $E(k_x, k_y)$, independent of k_x and k_y).

This transition is used to characterize the small-scale break $\xi_{\tau,s}$, which determines the lower size range of the detected cloud inhomogeneities and identifies the scale at which the measurements turn into white noise. To derive $\xi_{\tau,s}$, fits are applied to the two scale-invariant regimes of $E(k_x, k_y)$ (shown for E_b in Fig. 5i). Subsequently, the small scale break $\xi_{\tau,s}$ is determined as the intersection of those fits. The small scale break $\xi_{\tau,s}$ is connected to the pixel size, which depends on the distance between cloud and sensor. The corresponding k_x and k_y give $\xi_{\tau,s}$. $\xi_{\tau,s}(E_a)$ and $\xi_{\tau,s}(E_b)$ for case C-01 are at about 0.03 km ($\log_2 k_{x,y} \approx 5$). $\xi_{\tau,s}(E_a)$ and $\xi_{\tau,s}(E_b)$ of Case C-02 are in the length range of 0.09 km ($\log_2 k_{x,y} \approx 3.5$) and 0.03 km ($\log_2 k_{x,y} \approx 5$), respectively. $\xi_{\tau,s}(E_a)$ from case C-
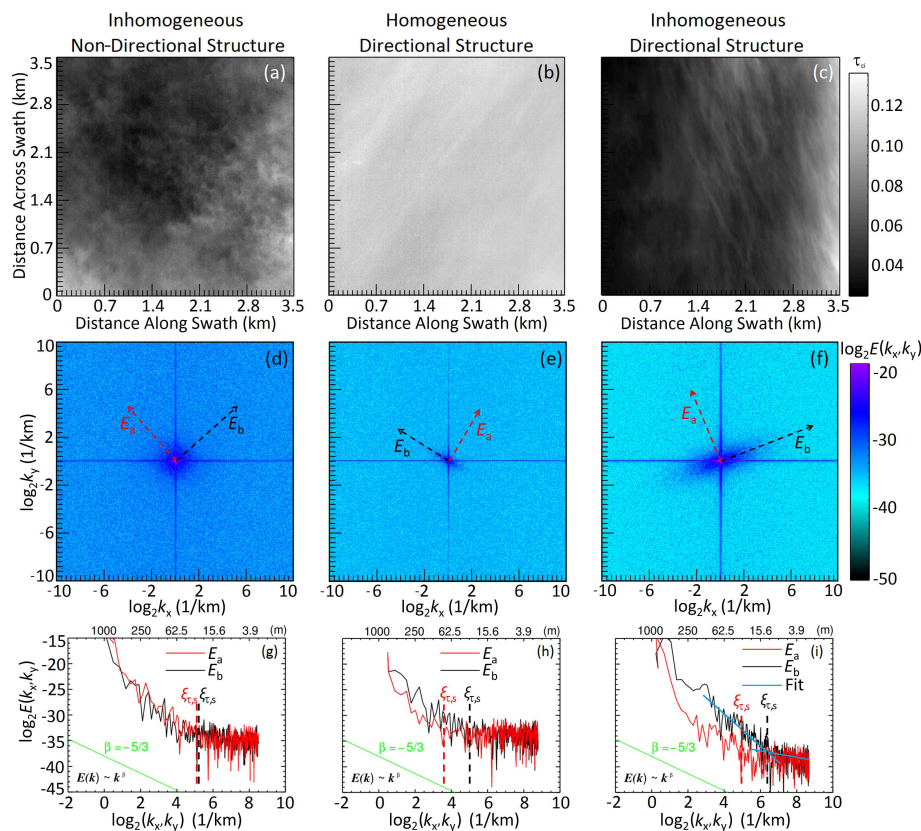
Atmospheric
Chemistry
and Physics
Discussions

Figure 5. (a-c) AisaEAGLE image (3.5 by 3.5 km), **(d-f)** 2D power spectral density $E(k_x, k_y)$, and **(g-i)** 1D power spectral density $E(k_x, k_y)$ across (red arrows, E_a) and along (black arrows, E_b) the prevailing direction of scale invariant areas for **(a), (d), (g)** inhomogeneous cloud without directional structure, **(b), (e), (h)** homogeneous cloud with slight directional structure, and **(c), (f), (i)** inhomogeneous cloud with distinct directional structure. The $\xi_{\tau,s}$ are marked by colored dashed lines.

03 is at about 0.03 km ($\log_2 k_{x,y} \approx 5$), while $\xi_{\tau,s}(E_b)$ is at about 0.01 km ($\log_2 k_{x,y} \approx 6.5$), which is already close to the pixel size. Thus, $\xi_{\tau,s}$ yields quantitatively larger values along the prevailing cloud structure than across.

Marshak et al. (1995) discussed that cloud inhomogeneity and horizontal photon transport are scale–dependent processes. The $E(k_x, k_y)$ of cloud optical and microphysical properties are proportional to k_x^β and k_y^β, where β is the slope of the power spectral density. At large scales, the $E(k_x, k_y)$ of e.g. I_λ, τ, LWC, or IWC follow Kolmogorov's $\beta = -5/3$ law of energy distribution in a turbulent fluid (Kolmogorov, 1941). At these scales, the variability in the radiation field follows the variability in LWC. Increasing cloud inhomogeneity causes a decrease of β of optical properties at smaller

Atmospheric
Chemistry
and Physics
Discussions

Open Access

325 scales, but not in β of microphysical properties. At scales influenced by horizontal photon transport, β may differ from -5/3 dependent on the cloud inhomogeneity that changes the magnitude of horizontal photon transport. Typically, this affects horizontal scales smaller than 1000 m. The higher the cloud inhomogeniety, the larger the deviation from -5/3. Thus the slope β at scales below 1000 m provides a measure of cloud inhomogeniety. Usually, the scale break ξ is used to quantify the devi-

330 ation from -5/3. In the following, the horizontal scale at which the power spectrum starts to deviate from the -5/3 law defines the large-scale break $\xi_{\tau,\mathrm{L}}$. The position of the large-scale break depends on the size of the horizontal cloud structures; more inhomogeneous clouds with larger variability on smaller scales yield smaller $\xi_{\tau,\mathrm{L}}$. For scales smaller than $\xi_{\tau,\mathrm{L}}$, the radiative smoothing leads to uncertainties in 1D cloud retrievals, where the horizontal photon transport is automatically neglected

335 (Cahalan, 1994; Marshak et al., 1998; Zinner et al., 2006; Varnai and Marshak, 2007).

A comparison of the $E(k_\mathrm{x}, k_\mathrm{y})$ to the -5/3 law in Figs. 5g to 5h shows that the analyzed scenes are to small to cover the larger scales, which are necessary to identify $\xi_{\tau,\mathrm{L}}$. The range of k_x and k_y is lower than $\xi_{\tau,\mathrm{L}}$ and $E(k_\mathrm{x}, k_\mathrm{y})$ already exhibit a steeper slope than $\beta = -5/3$. Therefore, the size of the selected areas was extended. Unfortunately, this is only possible for calculations of the DFT

340 along L_y (across swath). Calculations along L_x (swath) do not cover a sufficiently large distance to derive quantitative values for $\xi_{\tau,\mathrm{L}}$. Therefore, the following analysis is performed using 1D DFT along L_y only.

Figures 6a and 6b show the 1D DFT calculated across the swath for two typical cases of cirrus (CARRIBA case C-01) and Arctic stratus (VERDI case V-07). The two cases are selected, since

345 they exhibit a similar length L_y. For each line of the τ field (each swath pixel) $E(k_\mathrm{y})$ is calculated and the individual power spectra are overlayed as gray dots in Fig.6. To evaluate the resulting 1D Fourier spectra with reduced noise (rn) characteristics, the $E_\mathrm{rn}(k) \sim k^\beta$ are calculated with the use of octave binning, following the method proposed by Davis et al. (1996), Harris et al. (1997), and Schroeder (2004). Here, for the total number N of $E(k_\mathrm{y})$ the binning of k_y is specified by factors of

350 2^n with $n = 0,1,...,\log_2(N\text{-}2)$. Using those factors, bins for the wave numbers are generated and the corresponding $E(k_\mathrm{y})$ within the particular bin size are averaged. In addition to the reduced noise of $E(k_\mathrm{rn})$ compared to $E(k_\mathrm{y})$ the binning provides a uniform contribution of all scales to the average values.

The $E(k_\mathrm{rn})$ derived from the octave binning are included as green diamonds. The data of the oc-

355 tave binning were used to fit the spectra for different slopes in the different scale ranges. A green line indicates the $\beta = -5/3$ law. For large scales, the $E_\mathrm{rn}(k_\mathrm{y})$ (blue fit) approximately follow the $-5/3$ relation in both cases. The large-scale break ($\xi_{\tau,\mathrm{L}}$) is evident at the intersection between the blue and the red line. Here, the slope in the $E_\mathrm{rn}(k_\mathrm{y})$ becomes steeper. For the CARRIBA case $\xi_{\tau,\mathrm{L}} = 0.31$ km and the middle scale slope β_m decreases to -2.2. For the VERDI case $\xi_{\tau,\mathrm{L}} = 0.06$ km and β_m de-

360 creases to 2.2. The middle–scale slope β_m is a function of the inhomogeneity in the measured signals. With increasing inhomogeneity of the optical thickness τ, β_m decreases. Together with the smaller
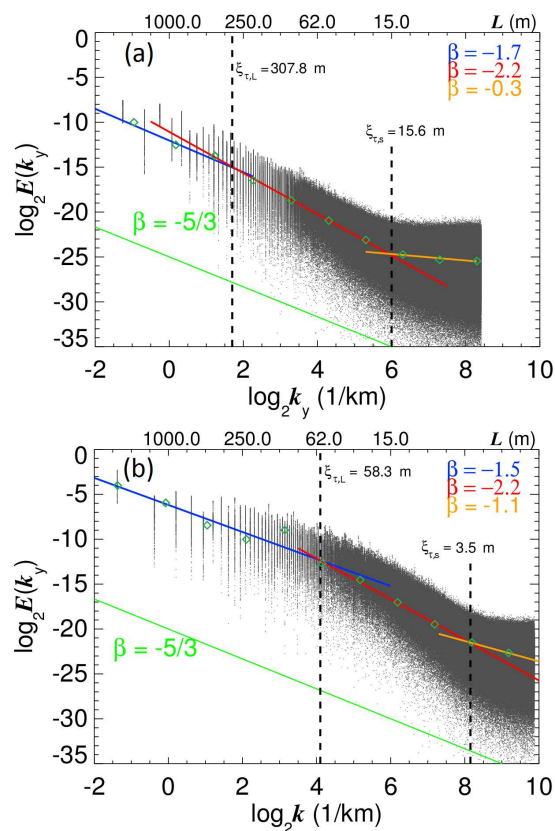
Atmospheric
Chemistry
and Physics
Discussions

Figure 6. 1D power spectral density $E(k_y)$ (gray dots) for each spatial pixel on the swath axis of the τ field from **(a)** case C-01 and **(b)** case V-07. Scale-invariant slopes β are marked with colored solid lines. The $E(k_{rn})$ derived from the octave binning are included as dark green diamonds. Scale breaks $\xi_{\tau,L}$ and $\xi_{\tau,s}$ are indicated by dashed lines.

$\xi_{\tau,L}$, this indicates that the stratus cloud of the VERDI case is more inhomogeneous compared to the cirrus cloud. As discussed above, $\xi_{\tau,s}$ is observed at the intersection between the fits for the middle (red, β_m) and small scales (orange, β_s). Due to the analysis of a significant larger distance compared to Fig. 5, it is highly uncertain to give quantitative numbers for $\xi_{\tau,s}$. Therefore, it is indicated only qualitatively. However, $\xi_{\tau,s}$ identifies at which scales the measurements turn into noise. The scale depends on the distance between sensor and cloud. For the sensor, noise dominated at scales two times pixel range, which corresponds to about 15 m for the cirrus observations (≈ 12 km cloud base altitude) and 3.5 m for the Arctic stratus observations where the aircraft was closer to cloud top (≈ 2 km distance).
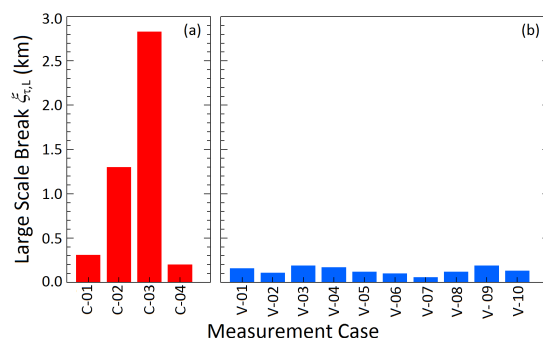
Atmospheric
Chemistry
and Physics
Discussions

Figure 7. 1D power spectral density $E(k_y)$ (gray dots) for each spatial pixel on the swath axis of the τ field from **(a)** case C-01 and **(b)** case V-07. Scale-invariant slopes β are marked with colored solid lines. The $E(k_{rn})$ derived from the octave binning are included as black diamonds. Scale breaks $\xi_{\tau,L}$ and $\xi_{\tau,s}$ are indicated by dashed lines.

Figure 7 illustrates $\xi_{\tau,L}$ for all available cloud cases from CARRIBA and VERDI. The values compare well with the derived decorrelation length ξ_τ derived in Sect. 4. Although the exact values of $\xi_{\tau,L}$ are not equal to ξ_τ, both are in the same size range for each individual case. Similar to ξ_τ given in Tab. 2, $\xi_{\tau,L}$ confirms that C-02 and C-03 are more homogeneous than C-01 and C-04. In general it was found that the cirrus observed during CARRIBA is more homogeneous than the Arctic stratus from VERDI.

An estimation of the uncertainty in the derived $\xi_{\tau,L}$ can be obtained from a comparison to investigations performed by Schröeder and Bennartz (2003). Amongst others, Schröeder and Bennartz (2003) investigated scale breaks as a function of wavelengths and absorption bands. Their results show uncertainties in a range of 3 % to 8 %. Schröeder and Bennartz (2003) derived those uncertainty values by subsetting the points of the power spectrum that are used for the slope fit. Using this method, they obtained a set of different slopes and scale breaks. The particular standard deviations of those sets are used as an uncertainty for the octave binning method. Applied to the VERDI cases, the 3 % to 8 % result in a maximum uncertainty of $\pm 5\,\mathrm{m}$ (V-07) to $\pm 15\,\mathrm{m}$ (V-03, V-09) in the derived $\xi_{\tau,L}$. For the CARRIBA cases the maximum uncertainty is in the range of 16 (C-04) to 226 m (C-03). However, especially case C-03 is characterized as rather homogeneous. Therefore, much lower uncertainty values are to be expected.

6 Summary and Conclusions

During the two field campaigns CARRIBA and VERDI, downward and upward solar spectral radiance ($I_\lambda^\downarrow$, $I_\lambda^\uparrow$) were measured with high spatial resolution ($< 10\,\mathrm{m}$), using the imaging spectrometer AisaEAGLE. The measured radiance fields were used to retrieve fields of τ, which were

Atmospheric
Chemistry
and Physics
Discussions

subsequently used to quantify horizontal cloud inhomogeneities. Imaging spectrometers such as AisaEAGLE help to identify and analyze the prevailing directional structure of cloud inhomogeneities.

395   Four cirrus cases collected during CARRIBA and ten Arctic stratus cases sampled during VERDI were studied in detail. The cloud inhomogeneity was quantified by three scalar 1D inhomogeneity parameters ρ_τ, S_τ, and χ_τ, as well as 1D and 2D autocorrelation functions, and Fourier analysis.

The results from the calculated scalar 1D inhomogeneity parameters ρ_τ and S_τ are in agreement with values given in the literature for similar cloud types. The calculated ρ_τ are in the range of
400   0.17–0.91 for the cirrus observed during CARRIBA and 0.15–0.34 for the Arctic stratus measured during VERDI. The literature values are in the range of 0.07–0.78 The inhomogeneity parameter S_τ exhibits values of 0.08 to 0.48 for CARRIBA and 0.07 to 0.20 for VERDI, which agrees with values of 0.03 to 0.3 given in literature. For χ_τ, the literature estimates values between ≈ 0.65 and 0.8, while the results from CARRIBA and VERDI are significantly larger. All values except for C-04
405   ($\chi_\tau = 0.63$) are in the range between 0.92 and 0.99. A further intercomparison between the results for the clouds encountered during CARRIBA and VERDI showed that all three scalar 1D inhomogeneity parameters exhibit values of similar magnitude for both cloud types; cirrus and Arctic stratus.

The 2D analysis of autocorrelation functions $P_\tau(L_\mathrm{x}, L_\mathrm{y})$ showed that the horizontal structure of clouds has to be considered when estimating the scalar 1D inhomogeneity parameters ρ_τ, S_τ, and
410   χ_τ. For both cloud cases the scalar 1D inhomogeneity parameters showed similar values, but significant differences resulting from the analysis of $P_\tau(L_\mathrm{x}, L_\mathrm{y})$, which additionally contain information about the horizontal structure of cloud inhomogeneities. Scalar 1D inhomogeneity parameters are not capable of differentiating the directional structure of clouds and may lead to misinterpretations of cloud inhomogeneity. From the squared autocorrelation functions $P_\tau^2(L_\mathrm{x}, L_\mathrm{y})$ the decorrelation
415   length ξ_τ was derived, which is a measure of the size range of the cloud inhomogeneities. The 2D analysis of $P_\tau^2(L_\mathrm{x}, L_\mathrm{y})$ revealed that ξ_τ is a function of the directional structure of the cloud inhomogeneities. Without knowledge of the directional structure of cloud inhomogeneities, no universally valid value for ξ_τ can be derived from the retrieved fields of τ. The differences in ξ_τ as derived from a 1D autocorrelation analysis along and across the prevailing structure of cloud inhomogeneities
420   reached up to 85 % and 77 % for CARRIBA and VERDI, respectively. It is concluded that the directional cloud structure has to be taken into account for a quantification of cloud inhomogeneities. The absolute values of ξ_τ were in the range of 0.43 km to 3.15 km for CARRIBA and 0.04 km to 0.28 km for VERDI.

3D radiative effects are quantified by applying 2D Fourier transformation to the retrieved fields
425   of τ. The power spectral densities $E(k_\mathrm{x,y})$ calculated from the Fourier Transform of $I_\lambda^\downarrow$ and $I_\lambda^\uparrow$ show evidence that 3D radiative effects did affect the radiation field of both cloud types, cirrus and Arctic stratus. For larger scales ($> 1000\,\mathrm{m}$), no horizontal photon transport was observed as the $E(k_\mathrm{x,y})$ followed Kolmogorov's -5/3 law. Approaching smaller scales ($< 1000\,\mathrm{m}$), the derived slopes become

steeper indicating radiative smoothing by cloud inhomogeneities and horizontal photon transport.

430 From the intersection of fits of the three slope regimes, the small-scale break $\xi_{\tau,\text{s}}$ (between small- and middle-scale slopes) and the large-scale break $\xi_{\tau,\text{L}}$ (between middle- and large-scale slopes) were derived. Similarly to the analysis using autocorrelation functions, $\xi_{\tau,\text{s}}$ depends on the directional structure of the cloud inhomogeneities. Due to a too small swath width, a similar analysis for $\xi_{\tau,\text{L}}$ could not be performed. However, the calculated $\xi_{\tau,\text{L}}$ along the image are comparable to the results

435 derived from the analysis of $P_\tau(L_\text{x}, L_\text{y})$. $\xi_{\tau,\text{L}}$ for CARRIBA was in the range of $0.20\,\text{km}$ to $2.83\,\text{km}$. For VERDI a range of $0.06\,\text{km}$ to $0.19\,\text{km}$ was covered by $\xi_{\tau,\text{L}}$.

In early studies, by e.g. Marshak et al. (1998) or Schroeder (2004), the scale dependence of cloud radiation measurements was analyzed along one direction (narrow pixel-lines) using 1D DFT. However, the resulting $E(k)$ are valid for the particular observation direction along the given path only.

440 Due to prevailing wind directions, clouds tend to evolve directional structures. In such cases, the calculated $E(k)$, β, $\xi_{\tau,\text{s}}$, and $\xi_{\tau,\text{L}}$ will only be valid for the whole cloud if the cloud structure exhibits a non-directional character (compare Figs. 2b and 3a). In all other cases, significant differences can be expected (compare Figs. 2d and 3b). Therefore, the directional structure of cloud inhomogeneities generally should be taken into account.

Atmospheric
Chemistry
and Physics
Discussions

References

455   **References**

Albrecht, B. A.: Aerosols, Cloud Microphysics, and Fractional Cloudiness, Science, 245, 1227–1230,
        http://www.sciencemag.org/content/245/4923/1227.abstract, 1989.

Barlakas, V., Macke, A., and Wendisch, M.: SPARTA - Solver for Polarized Atmospheric Radiative Trans-
        fer Applications: Introduction and application in Saharan dust fields, J. Quant. Spectr. & Rad. Trans.,
460   doi:10.1016/j.jqsrt.2016.02.019, http://dx.doi.org/10.1016/j.jqsrt.2016.02.019, 2016.

Bierwirth, E., Ehrlich, A., Wendisch, M., Gayet, J.-F., Gourbeyre, C., Dupuy, R., Herber, A., Neuber, R., and
        Lampert, A.: Optical thickness and effective radius of Arctic boundary-layer clouds retrieved from airborne
        nadir and imaging spectrometry, Atmos. Meas. Tech., 6, 1189–1200, doi:10.5194/amt-6-1189-2013, 2013.

Cahalan, R.: Bounded cascade clouds: albedo and effective thickness, Nonlin. Proc. Geophys., 1, 1994.

465   Cahalan, R. and Snider, J.: Marine stratocumulus structure, Remote Sens. Environ., 28, 95–107, 1989.

Carlin, B., Fu, Q., Lohmann, U., Mace, G., Sassen, K., and Comstock, J.: High-cloud horizontal inhomogeneity
        and solar albedo bias, J. Climate, 15, 2321–2339, 2002.

Choi, Y.-S. and Ho, C.-H.: Radiative effect of cirrus with different optical properties over the tropics in MODIS
        and CERES observations, Geophys. Res. Lett., 33, doi:10.1029/2006GL027 403, 2006.

470   Davis, A., Marshak, A., Wiscombe, W., and Cahalan, R.: Scale invariance in liquid water distributions in marine
        stratocumulus. Part I: Spectral properties and stationarity issues, J. Atmos. Sci., 53, 1538–1558, 1996.

Davis, A., Cahalan, R., Spinhirne, D., McGill, M., and Love, S.: Off-beam Lidar: an emerging technique in
        cloud remote sensing based on radiative green-function theory in the diffusion domain, Phys. Chem. Earth
        (B), 24, 177–185, 1999.

475   Francis, P., Hignett, P., and Macke, A.: The retrieval of cirrus cloud properties from aircraft multi-spectral
        reflectance measurements during EUCREX '93, Quart. J. Roy. Meteor. Soc., 124, 1273–1291, 1998.

Garrett, T. J., Gerber, H., Baumgardner, D. G., Twohy, C. H., and Weinstock, E. M.: Small, highly reflective ice
        crystals in low-latitude cirrus, Geophys. Res. Lett., 30, doi:10.1029/2003GL018 153, 2003.

Geleyn, J. F. and Hollingsworth, A.: An economical, analytical method for the computation of the interaction
480   between scattering and line absorbtion of radiation, Contr. Atmos. Phys., 52, 1–16, 1979.

Hanus, J., Malenovsky, Z., Homolova, L., Veroslav, K., Petr, L., and Pavel, C.: Potential of the VNIR Airborne
        hyperspectral system AISA Eagle, in: Symposium GIS Ostrava, (CZ), 2008.

Harris, D., Seed, A., Menabde, M., and Austin, G.: Factors affecting multiscaling analysis of rainfall time series,
        Nonlin. Proc. Geophys., 4, 137–156, 1997.

485   Hill, P. G., Hogan, R. J., Manners, J., and Petch, J. C.: Parametrizing the horizontal inhomogeneity of ice water
        content using CloudSat data products, Q. J. R. Meteorol. Soc., 138, 1784–1793, 2012.

Hogan, R. and Illingworth, A.: Deriving cloud overlap statistics from radar, Q. J. R. Meteorol. Soc., 126, 2903–
        2909, 2000.

Huang, D. and Liu, Y.: A novel approach for introducing cloud spatial structure into cloud radiative transfer
490   parameterizations, Environ. Res. Lett., 9, 124 022, 2014.

IPCC: Climate Change 2013: The Physical Science Basis, Cambridge University Press, 2013.

Iwabuchi, H.: Effects of cloud horizontal inhomogeneity on optical remote sensing of cloud parameters, Ph.D.
        thesis, Center for Atmospheric and Oceanic Studies, Graduate School of Science, Tokohu University, 2000.

Iwabuchi, H. and Hayasaka, T.: Effects of cloud horizontal inhomogeneity on the optical
495   thickness retrieved from moderate-resolution satellite data, J. Atmos. Sci., 59, 2227–2242,
        doi:10.1175/1520-0469(2002)059<2227:EOCHIO>2.0.CO;2, 2002.

Kolmogorov, A.: Die Energiedissipation für lokalisotrope Turbulenz, Dokl. Akad. Nauk SSSR, 32, 16–18,
        Nachdruck in: H. Goering Hrsg., 1958: Statistische Theorie der Turbulenz., Akademie–Verlag, Berlin, 71–
        76., 1941.

500 Loeb, N. and Davies, R.: Observational evidence of plane parallel model biases: Apparent dependence of cloud
        optical depth on solar zenith angle, J. Geophys. Res., 101, 1621–1634, doi:10.1029/95JD03298, 1996.

Loeb, N. G., Wielicki, B. A., Doelling, D. R., Smith, G. L., Keyes, D. F., Kato, S., Manalo-Smith, N., and
        Wong, T.: Toward Optimal Closure of the Earth's Top-of-Atmosphere Radiation Budget, Journal of Climate,
        22, 748–766, doi:10.1175/2008JCLI2637.1, 2009.

505 Marshak, A., Davis, A., Wiscombe, W., and Cahalan, R.: Radiative smoothing in fractal clouds, J. Geophys.
        Res., 100, 26 247–26 261, 1995.

Marshak, A., Davis, A., Cahalan, R., and Wiscombe, W.: Nonlocal independent pixel approximation: Direct
        and inverse problems, IEEE Trans. Geosci. Remote Sens., 36, 192–204, 1998.

Oreopoulos, L. and Cahalan, R. F.: Cloud Inhomogeneity from MODIS, J. Climate, 18, 5110–5124, 2005.

510 Oreopoulos, L., Cahalan, R., Marshak, A., and Wen, G.: A new normalized difference cloud retrieval technique
        applied to Landsat radiances over the Oklahoma ARM site, J. Appl. Meteorol., 39, 2305–2321, 2000.

Pinsky, M. and Khain, A.: Fine structure of cloud droplet concentration as seen from Fast-FSSP measurements.
        Part II: Results of in-situ observations, J. Appl. Meteorol., 42, 65–73, 2003.

Rossow, W. and Schiffer, R.: Advances in understanding clouds from ISCCP, Bull. Amer. Meteorol. Soc., 80,
515   2261–2287, 1999.

Rozwadowska, A. and Cahalan, R. F.: Plane-parallel biases computed from inhomogeneous Arctic clouds and
        sea ice, J. Geophys. Res., 107, 4384, 2002.

Schäfer, M., Bierwirth, E., Ehrlich, A., Heyner, F., and Wendisch, M.: Retrieval of cirrus optical thickness and
        assessment of ice crystal shape from ground-based imaging spectrometry, Atmos. Meas. Tech., 6, 1855–
520   1868, doi:10.5194/amt-6-1855-2013, 2013.

Schäfer, M., Bierwirth, E., Ehrlich, A., Jäkel, E., and Wendisch, M.: Observations and simulations of three-
        dimensional radiative interactions between Arctic boundary layer clouds and ice floes, Atmos. Chem. Phys.
        Discuss., 15, 1421–1469, doi:10.5194/acpd-15-1421-2015, 2015.

Schroeder, M.: Multiple scattering and absorption of solar radiation in the presence of three-dimensional cloud
525   fields, Ph.D. thesis, Fachbereich Geowissenschaften der Freien Universität Berlin, 2004.

Schröeder, M. and Bennartz, R.: Impact of gas absorption and surface albedo on cloud radia-
        tive smoothing, Geophysical Research Letters, 30, 1168–1171, doi:10.1029/2002GL016523,
        http://dx.doi.org/10.1029/2002GL016523, 2003.

Shonk, J. K. P. and Hogan, R. J.: Tripleclouds: an efficient method for representing cloud inhomogeneity in 1D
530   radiation schemes by using three regions at each height, J. Clim., 21, 2352–2370, 2008.

Shonk, J. K. P., Hogan, R. J., and Manners, J.: Impact of improved representation of horizontal and vertical
        cloud structure in a climate model, J. Clim., 38, 2365–2376, doi:10.1007/s00382-011-1174-2, 2011.

Atmospheric
Chemistry
and Physics
Discussions

Open Access

EGU

Siebert, H., Bethke, J., Bierwirth, E., Conrath, T., Dieckmann, K., Ditas, F., Ehrlich, A., Farrell, D., Hartmann, S., Izaguirre, M. A., Katzwinkel, J., Nuijens, L., Roberts, G., Schäfer, M., Shaw, R. A., Schmeissner, T.,

535   Serikov, I., Stevens, B., Stratmann, F., Wehner, B., Wendisch, M., Werner, F., and Wex, H.: The fine–scale structure of the trade wind cumuli over Barbados – an introduction to the CARRIBA project, Atmos. Chem. Phys., 13, 10 061–10 077, doi:doi:10.5194/acp-13-10061-2013, 2013.

Slingo, A.: Sensitivity of the Earths Radiation Budget to Changes in Low Clouds, Nature, 343, 49–51, 1990.

Stephens, G.: Cloud feedbacks in the climate system: A critical review, J. Climate, 18, 237–273, 2005.

540   Stocker, T. F., Qin, D., Plattner, G. K., Tignor, M., Allen, S. K., Boschung, J., Nauels, A., Xia, Y., Bex, V., and Midgley, P. M., eds.: Climate Change 2013: The Physical Science Basis. Working Group I Contribution to the Fifth Assessment Report of the Intergovernmental Panel on Climate Change, Cambridge University Press, UK, 2013.

Szczap, F., Isaka, H., Saute, M., and Guillemet, B.: Effective radiative properties of bounded cascade non-
545   absorbing clouds: Definition of the equivalent homogeneous cloud approximation, J. Geophys. Res., 105, 20 617–20 633, 2000.

Varnai, T. and Marshak, A.: View angle dependence of cloud optical thicknesses retrieved by Moderate Resolution Imaging Spectroradiometer (MODIS), J. Geophys. Res., 112, D06 203, doi:10.1029/2005JD006912, 2007.

550   Wendisch, M., Yang, P., and Ehrlich, A., eds.: Amplified climate changes in the Arctic: Role of clouds and atmospheric radiation, vol. 132, chap. 1, pp. 1–34, Sitzungsberichte der Sächsischen Akademie der Wissenschaften zu Leipzig, Mathematisch-Naturwissenschaftliche Klasse, S. Hirzel Verlag, 2013.

Zinner, T., Mannstein, H., and Tafferner, A.: Cb-TRAM: Tracking and monitoring severe convection from onset over rapid development to mature phase using multi-channel Meteosat-8 SEVIRI data, Meteorology
555   and Applied Physics, submitted, 2006.

Zuidema, P. and Evans, K.: On the validity of the independent pixel approximation for boundary layer clouds observed during ASTEX, J. Geophys. Res., 103, 6059–6074, 1998.